Cement and Concrete Research 94 (2017) 24–35

Contents lists available at ScienceDirect

Cement and Concrete Research

journal homepage: www.elsevier.com/locate/cemconres

Corrosion induced cracking modelled by a coupled transport-structural approach

Caroline Fahy[a], Simon J. Wheeler[a], Domenico Gallipoli[b], Peter Grassl[a,*]

[a] School of Engineering, University of Glasgow, Glasgow, UK
[b] Laboratoire SIAME, Université de Pau et des Pays de l'Adour, Anglet, France

ARTICLE INFO

Article history:
Received 9 August 2016
Received in revised form 9 December 2016
Accepted 10 January 2017
Available online xxxx

ABSTRACT

Transport of corrosion products into pores and cracks in concrete must be considered when predicting corrosion induced cracking in reinforced concrete structures, since this transport significantly delays the onset of cracking and spalling by reducing the amount of radial displacement imposed on the concrete at the steel/concrete interface. We aim to model this process by means of a coupled transport-structural approach, whereby the transport of corrosion products is determined by a pressure gradient generated by the confined volumetric expansion due to the transformation of steel into corrosion products. This pressure driven transport was studied by using both an axisymmetric thick-walled cylinder model and a network approach. The network approach was then applied to corrosion induced cracking experiments reported in the literature.

1. Introduction

Corrosion of steel reinforcement is one of the most commonly encountered deterioration mechanisms leading to cracking of concrete [6]. The process of corrosion induced deterioration is commonly divided into initiation and propagation phases [28], whereby the propagation is characterised by the progression from corrosion initiation to surface cracking, spalling and eventually structural collapse either due to loss of anchorage or reinforcement rupture (Fig. 1). The present work is focused on the propagation phase by modelling the transport of corrosion products into the concrete and its influence on the process of corrosion induced cracking. Corrosion in reinforced concrete involves the transformation of steel reinforcement into corrosion products, which occupy greater volume than the original steel. The ratio of the volumes of corrosion products and steel can vary from less than two to more than six [6]. This volume expansion results in internal pressure acting on the concrete, which is equilibrated by circumferential tensile stresses leading to cracks in and potentially spalling of the concrete. Understanding corrosion induced cracking in concrete is difficult because of multiple interacting processes and phenomena, such as the transport of corrosion products into pores and cracks, the spatial distribution of steel areas affected by corrosion, compaction of corrosion products, the influence of the chemical environment on the rust products, and creep, shrinkage, hardening and cracking of concrete. The process of corrosion induced cracking involves strong coupling between the electro-chemical process of the generation of corrosion products (modelled as a fluid in this work) and their structural confinement by the surrounding concrete. The build up of fluid pressure due to this coupling results in the transport of corrosion products into pores and cracks in the concrete, which must be considered when predicting corrosion induced cracking in reinforced concrete structures, since this transport significantly delays the onset of cracking.

Physical tests on corrosion induced cracking have been reported for single and multiple reinforcement bars in [1,2,18,24]. Experimental studies in [31] and [16] have shown that corrosion products are transported into pores and cracks. Modelling approaches are categorised into models for specimens with simple geometries, such as thick-walled cylinders, for which solutions can be obtained in compact form [3,14,21] and numerical models applicable to general geometries and boundary conditions [15,17,20,23,26,27].

In both axisymmetric and general numerical models, the transport of corrosion products into the concrete has been considered in different ways. In many approaches, a porous zone was considered which had to be filled before the volume expansion due to the transformation of steel into corrosion products started to generate pressure in the surrounding concrete [9,14]. In other studies, it was proposed to fill voids and cracks once corrosion induced cracking had started [7,26,27]. These modelling approaches use adhoc rules to describe the penetration of the rust. In [20], diffusion is used to describe the transport of rust into the concrete. None of the above approaches link the transport to the pressure build up due to the

* Corresponding author.
E-mail address: peter.grassl@glasgow.ac.uk (P. Grassl).

http://dx.doi.org/10.1016/j.cemconres.2017.01.007

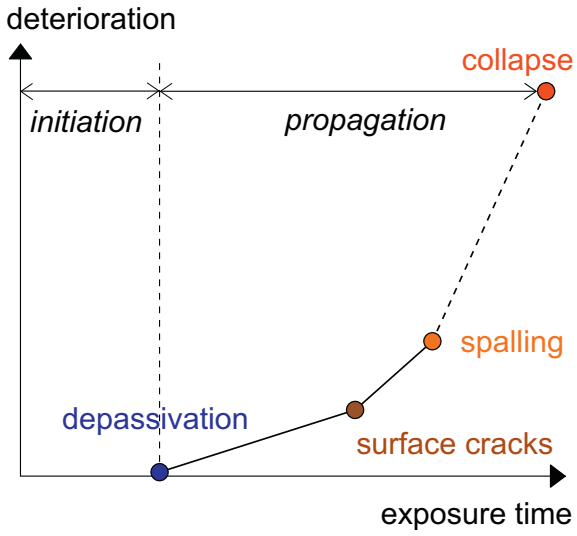

Fig. 1. Corrosion induced cracking: service life definition after Tuutti [28].

structural confinement of the corrosion products. The aim of the present work is to model the mechanics of the transport of rust into concrete by a transport-structural approach, whereby the fluid composed of corrosion products is transported into the concrete by means of a pressure gradient originating from the volume expansion due to the transformation from steel into corrosion products. The assumption that corrosion products can be treated as fluid has already been proposed in [17], where only structural analyses were performed. Most approaches model corrosion to occur uniformly around the reinforcement bar, which was also assumed in the present study. However, it should be kept in mind that the spatial distribution around the reinforcement bar can have a strong effect on surface cracking as shown in [32].

The transport-structural modelling of corrosion induced cracking was introduced here both in an axisymmetric thick-walled cylinder approach for describing the stage from initiation to surface cracking and a 2D discrete network approach, which conceptually is capable of describing the full propagation phase (Fig. 1). The axisymmetric thick-walled cylinder model is an extension of the approach reported in [21]. The main difference to [21] is that the structural model is extended to a transport-structural approach. The numerical network model belongs to the group of discrete element approaches, for which the connectivity between elements remains the same during the analysis [5,8,25]. They are often also called lattice or rigid-body-spring network models. This type of network models has been shown to be capable of describing fracture and transport in concrete mesh-independently and modelling of the coupling of fracture and transport [4,11,13].

2. Corrosion products at steel/concrete interface

The pressure generated by the confinement of corrosion products is used to model the transport of these products into the cracked porous concrete. The main assumptions of this approach are that the corrosion products form an incompressible fluid with a time independent viscosity. Furthermore, concrete is assumed to be fully saturated and Biot's coefficient for the porous concrete is assumed to be zero, i.e. the fluid pressure within the concrete does not affect the mechanical stress. However, the generation of corrosion products at the steel/concrete interface results in pressure build up.

In laboratory experiments, corrosion of reinforcement is often accelerated by applying a current density i_{cor} to the reinforced concrete specimens. In this setup, the change of loss of steel radius dx_{cor} is related to the current density i_{cor} through Faraday's law, where

$$dx_{cor} = 0.0315 i_{cor} dt \tag{1}$$

in which 0.0315 is a factor converting the units of i_{cor} from $\mu A/cm^2$ into μm/days as used in [17]. This relationship is used in the present study to relate the time increment dt to the increment of loss of steel layer dx_{cor}. This steel layer is then related to a layer of corrosion products by means of an expansion factor. The overall approach for the modelling of the volume expansion associated with the transformation from steel into corrosion products is to apply a part of the corrosion product layer as a displacement change du_{cor} at the interface between the steel and concrete, which results in a reactive pressure P_{fi} in the structural part of the model. The remaining part is equal to the volume of corrosion products transported into the pores and cracks of the concrete. The prescribed displacement change du_{cor} was modelled in different ways. For the axisymmetric thick-walled cylinder model, the displacement at the inner boundary was directly applied, since the reinforcement was assumed to be rigid and was not modelled. For the network model, in which reinforcement, interface and concrete are discretised, the volume expansion is modelled through an eigendisplacement at the interface. If the reinforcement and interface are assumed to be infinitely stiff, this is equivalent to prescribing the displacement du_{cor} directly. This allowed for comparing the results of the axisymmetric and 2D network model. This pressure is then used to determine the flow of corrosion products into the concrete by the transport part of the model. With this approach, the structural analysis is independent of the transport part.

In Fig. 2, the geometrical meaning of the different components is illustrated, where r_i is the initial radius of the reinforcement bar (the inner radius of the thick-walled cylinder), x_{cor} is the thickness of steel that has been removed at time t due to corrosion, α is an expansion factor, describing the volume increase on transformation from steel to corrosion products, and u_{cor} is the prescribed radial displacement at the steel/concrete interface.

For a time change dt, the volume balance is

$$\alpha dx_{cor} = dx_{cor} + du_{cor} + q dt \tag{2}$$

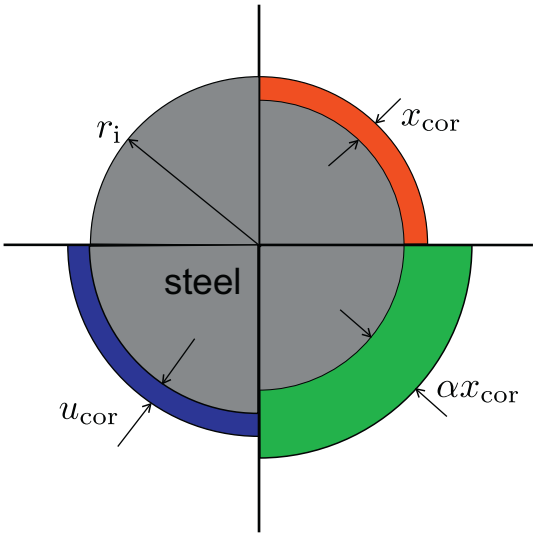

Fig. 2. Corrosion induced cracking: (b) steel reinforcement bar with layers illustrating the split into different corrosion product components.

where $q = Q/(2\pi r_i)$ is the flux of corrosion products transported into the pores and cracks of the concrete (i.e. the flow rate per unit area of corrosion products, where Q is the total flow rate assuming unit out-of-plane thickness). For the balance of Eq. (2), it is assumed that x_{cor}, αx_{cor} and u_{cor} are much smaller than the radius of the reinforcement bar, so that, for instance, the volume of the steel loss around the reinforcement bar is approximated as $x_{cor} 2\pi r_i$. The flux q is a function of the pressure generated by the confinement of corrosion products.

Substituting dt from Eq. (1) in Eq. (2) and solving for dx_{cor} give

$$dx_{cor} = \frac{du_{cor}}{\alpha - 1 - q/(0.0315 i_{cor})} \tag{3}$$

Thus, if for a prescribed displacement du_{cor} the flux of corrosion products q is determined, the change of radial loss of steel dx_{cor} is calculated from Eq. (3). The input parameters for this approach are the current density (corrosion rate) i_{cor} and the expansion factor α. The prescribed radial displacement du_{cor} and the flux q are determined by means of the axisymmetric and network models described in the following sections, which require additional input parameters.

3. Axisymmetric thick-walled cylinder model

A thick-walled cylinder is modelled assuming axisymmetry and using orthotropic elasticity following the work in [21,29]. The main approach is to divide the thick-walled cylinder into an inner cracked and outer uncracked region (Fig. 3). For the cracked region, orthotropic elasticity is used [21], whereas the uncracked region is modelled with isotropic elasticity [29]. The orthotropy for the cracked cylinder is introduced by reducing the tangential Young's modulus by means of a scalar damage model, which is driven by an exponential stress-crack opening law.

The main equation for the structural part of the thick-walled cylinder model for both cracked and uncracked regions is the equilibrium equation

$$\sigma_r + \frac{d\sigma_r}{dr} r - \sigma_\theta = 0 \tag{4}$$

Here, r is the radial coordinate, and σ_r and σ_θ are the radial and circumferential stress, respectively, which are defined as

$$\sigma_r = \frac{1}{1 - \nu_{r\theta}\nu_{\theta r}} \left(E_r \varepsilon_r + \nu_{r\theta} E_\theta \varepsilon_\theta\right) \tag{5}$$

and

$$\sigma_\theta = \frac{1}{1 - \nu_{r\theta}\nu_{\theta r}} \left(E_\theta \varepsilon_\theta + \nu_{\theta r} E_r \varepsilon_r\right) \tag{6}$$

together with the condition that

$$\nu_{\theta r} = \nu_{r\theta} \frac{E_\theta}{E_r} \tag{7}$$

Here, E_θ and E_r are the circumferential and radial Young's moduli, respectively. Furthermore, $\varepsilon_r = du/dr$ and $\varepsilon_\theta = u/r$ are the radial and circumferential strain, respectively, where u is the radial displacement. The parameters $\nu_{r\theta}$ and $\nu_{\theta r}$ are the Poisson's ratios of the orthotropic material. The ratio E_θ/E_r is related to the damage parameter ω as

$$\frac{E_\theta}{E_r} = 1 - \omega \tag{8}$$

Setting Eqs. (5), (6) and (8) into the equilibrium equation in Eq. (4), and assuming that $\nu_{\theta r} = \nu_{r\theta} = 0$, gives the second order ordinary differential equation

$$\frac{d^2u}{dr^2} + \frac{1}{r}\frac{du}{dr} - (1 - \omega)\frac{u}{r^2} = 0 \tag{9}$$

Thus, damage is introduced by reducing only the tangential Young's modulus. For $\nu_{r\theta} \neq 0$, $\nu_{\theta r} \neq 0$ and $\omega \neq 0$, Eq. (9) would result in a more complex second order differential equation. For the uncracked region, $\omega = 0$ so that $E_\theta = E_r = E$ and Eq. (9) is linear. For this case, Eq. (9) is valid for any Poisson's ratio. For the cracked region, ω is a nonlinear function of the radius and the radial displacement. It is determined by setting the circumferential stress equal to the stress obtained from an exponential stress-crack opening law of the form

$$\sigma_\theta = f_t \exp\left(-\frac{\omega \varepsilon_\theta}{\varepsilon_f}\right) \tag{10}$$

which is controlled by the inelastic strain

$$\varepsilon_f = n_c \frac{w_f}{l_c} \tag{11}$$

The parameter w_f is the crack opening threshold in the exponential stress crack opening law which is related to the fracture energy G_F

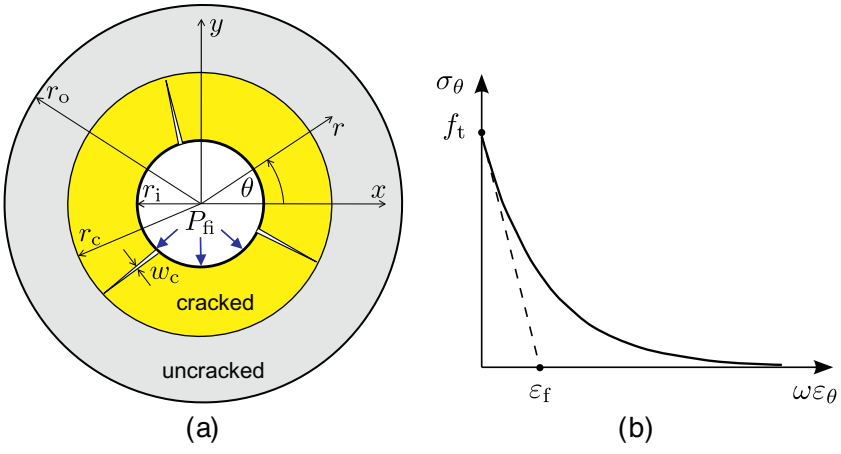

Fig. 3. Axisymmetric model: (a) thick-walled cylinder divided into an inner cracked and outer uncracked part, (b) exponential stress crack opening curve.

and the tensile strength f_t as $w_f = G_F/f_t$, and n_c is the number of cracks assumed to be present in the thick-walled cylinder. Furthermore, $l_c = 2\pi r$.

For each part of the cylinder, two boundary conditions are required to solve the second order ordinary differential equation. For the outer uncracked cylinder, the conditions are that the radial stress at the outer boundary is equal to zero ($\sigma_r(r = r_o) = 0$) and the tangential stress at the boundary between cracked and uncracked regions is equal to the tensile strength ($\sigma_\theta(r = r_c^+) = f_t$). The two conditions for the cracked cylinder are that the two radial stresses at the boundary between cracked and uncracked regions are equal ($\sigma_r(r = r_c^+) = \sigma_r(r = r_c^-)$) and the tangential stress at the boundary between cracked and uncracked regions is equal to the tensile strength ($\sigma_\theta(r = r_c^-) = f_t$). For the uncracked part, Eq. (9) can be solved explicitly. However, for the cracked part, a finite difference scheme is used to obtain the solution numerically. The solution for the radial displacement u in the two regions are obtained for an increasing radius r_c. From u, the radial and tangential stresses and strains are computed. The radial displacement u at $r = r_i$, i.e. at the inner boundary of the cylinder, is equal to the eigendisplacement u_{cor} in Section 2.

The transport part of the axisymmetric model is an extension of the approach described in [13] to the case of a cracked cylinder. The influence of cracks on the transport is described by the cubic law [30], which is a function of the crack opening. This crack opening is determined from the structural part as

$$w_c = \frac{l_c}{n_c}\omega\varepsilon_\theta \tag{12}$$

According to [13], the radial stress at the inner boundary ($\sigma_r(r = r_i)$) is set equal to the fluid pressure P_{fi} at the inner boundary (tension positive). The spatial gradient of the fluid pressure P_f in the radial direction is related by Darcy's law to the total flow rate Q through the cylinder as

$$dP_f = \frac{\mu}{\kappa}\frac{Q}{2\pi r}dr \tag{13}$$

where μ is the dynamic viscosity of the corrosion products, which is the fluid transported through the thick-walled cylinder. Furthermore, κ is the permeability which is composed of an uncracked contribution κ_0 and a cracked contribution $\kappa_c(r)$ as $\kappa = \kappa_0 + \kappa_c(r)$, whereby

$$\kappa_c = n_c\xi\frac{w_c^3}{12l_c} \tag{14}$$

is the cubic law reduced by a factor ξ taking into account the influence of fracture roughness on the crack permeability. The required input parameters of the axisymmetric model assuming $\nu_{r\theta} = \nu_{\theta r} = 0$ are E_r, n_c, f_t, G_F, κ, μ and ξ.

4. Network model

The network model used in this study is based on the approach presented in [13], extended to the modelling of the influence of cracking on the permeability. The domain is discretised by a 2D (out-of-plane direction corresponds to the axis of a reinforcement bar) structural and transport network, which is generated by dual Voronoi and Delaunay tessellations based on an irregular set of randomly placed points restricted by a minimum distance d_{min}. The structural and transport elements are placed on the edges of Delaunay triangles and Voronoi polyhedra, respectively (Fig. 4a).

In the following sections, the element and material formulations of the structural and transport lattices are discussed.

4.1. Structural network model

For the 2D structural analysis, the general equilibrium equation for the quasi-static case without body forces is

$$\nabla\boldsymbol{\sigma}^c = \boldsymbol{0} \tag{15}$$

where ∇ is the divergence operator and $\boldsymbol{\sigma}^c$ is the continuum stress tensor. This equilibrium equation is approximated by a network of structural elements shown by solid lines in Fig. 4a. Each element connects two nodes, which possess three degrees of freedom, namely two translations and one rotation. They are related to a discontinuity at the mid-point C of the mid-cross-section (Fig. 4b). The distance e between the centre C of the mid-cross-section and the mid-point of the element is defined to be positive if it is located on the left of the element. The degrees of freedom of one element $\mathbf{u}_e$ are split into translational and rotational degrees of freedom as $\mathbf{u}_e = \{\mathbf{u}_t^T, \mathbf{u}_r^T\}^T$ where $\mathbf{u}_t = \{u_1, v_1, u_2, v_2\}^T$ and $\mathbf{u}_r = \{\phi_1, \phi_2\}^T$. The degrees of

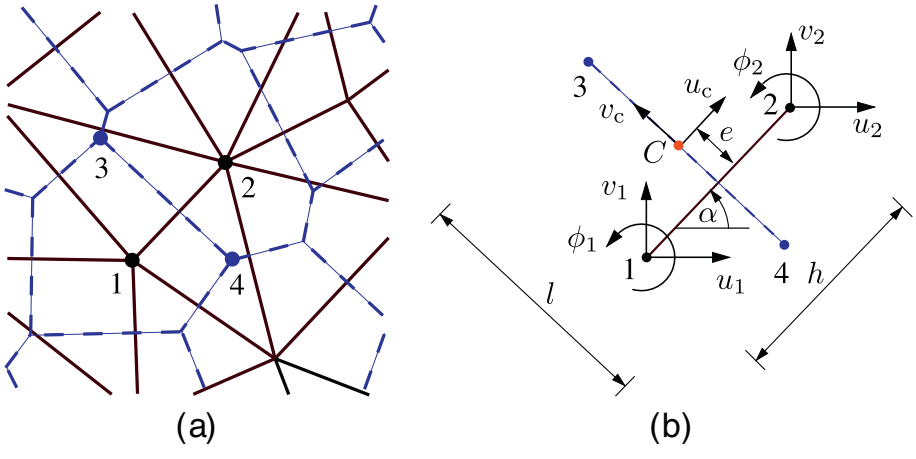

Fig. 4. Network model: (a) discretisation based on dual Delaunay and Voronoi tessellation, (b) structural and transport elements.

freedom $\mathbf{u}_t$ and $\mathbf{u}_r$ are related to the displacement discontinuities $\mathbf{u}_c = \{u_c, v_c\}^T$ at the mid-point C of the mid-cross-section as

$$\mathbf{u}_c = \mathbf{B}_t\mathbf{u}_t + \mathbf{B}_r\mathbf{u}_r \tag{16}$$

where

$$\mathbf{B}_t = \begin{pmatrix} -\cos\alpha & -\sin\alpha & \cos\alpha & \sin\alpha \\ \sin\alpha & -\cos\alpha & -\sin\alpha & \cos\alpha \end{pmatrix} \tag{17}$$

with the orientation α shown in Fig. 4b, and

$$\mathbf{B}_r = \begin{pmatrix} -e & -e \\ -h/2 & -h/2 \end{pmatrix} \tag{18}$$

The stiffness matrix of the lattice element has the form

$$\mathbf{K} = \frac{A}{h}\begin{pmatrix} \mathbf{B}_t^T\mathbf{D}\mathbf{B}_t & \mathbf{B}_t^T\mathbf{D}\mathbf{B}_r \\ \mathbf{B}_r^T\mathbf{D}\mathbf{B}_t & \mathbf{B}_r^T\mathbf{D}\mathbf{B}_r \end{pmatrix} + \begin{pmatrix} \mathbf{0} & \mathbf{0} \\ \mathbf{0} & \mathbf{K}_r \end{pmatrix} \tag{19}$$

Here, $\mathbf{D}$ is the material stiffness and $\mathbf{K}_r$ is the rotational stiffness representing resistance of the mid-cross-section to bending, which is

$$\mathbf{K}_r = \frac{(1-\omega)}{h}\begin{pmatrix} EI & EI \\ EI & EI \end{pmatrix} \tag{20}$$

The damage factor $1-\omega$ in the rotational stiffness $\mathbf{K}_r$ ensures that the stiffness reduces to zero for damage increasing to one.

The displacement discontinuities $\mathbf{u}_c$ are transformed into strains as $\boldsymbol{\varepsilon} = \mathbf{u}_c/h = \{\varepsilon_n, \varepsilon_s\}^T$, where h is the distance between the element nodes (Fig. 4b). The strains are related to the stresses $\boldsymbol{\sigma} = \{\sigma_n, \sigma_s\}^T$ by an isotropic damage model. The subscripts n and t refer to the normal and shear components of the strain and stress vector. The stress-strain law is

$$\boldsymbol{\sigma} = (1-\omega)\,\mathbf{D}\boldsymbol{\varepsilon} \tag{21}$$

Here, $\mathbf{D}$ is the elastic stiffness defined as

$$\mathbf{D} = \begin{pmatrix} E & 0 \\ 0 & \gamma E \end{pmatrix} \tag{22}$$

where E and γ are model parameters, which are related to the continuum Young's modulus E_c and Poisson's ratio ν. For the special case of $\gamma = 1$ the continuum parameters are $E_c = E$ and $\nu = 0$, which were used in the analyses in this work.

The damage parameter ω is a function of a history variable κ, which is determined by the loading function

$$f(\boldsymbol{\varepsilon}, \kappa) = \varepsilon_{eq}(\boldsymbol{\varepsilon}) - \kappa \tag{23}$$

and the loading-unloading conditions

$$f \le 0, \quad \dot{\kappa} \ge 0, \quad \dot{\kappa} f = 0 \tag{24}$$

The equivalent strain ε_{eq} in Eq. (23) is defined as

$$\varepsilon_{eq}(\varepsilon_n, \varepsilon_s) = \frac{1}{2}\varepsilon_0(1-c) + \sqrt{\left(\frac{1}{2}\varepsilon_0(c-1) + \varepsilon_n\right)^2 + \frac{c\gamma^2\varepsilon_s^2}{s^2}} \tag{25}$$

where ε_0, c and s are model parameters, which are directly related to the strength and stiffness of the equivalent continuum of the lattice elements.

For $\varepsilon_{eq} = \varepsilon_0$, this equivalent strain definition results in an elliptic strength envelope shown in Fig. 5. For pure tension, the stress is limited by the tensile strength $f_t = E\varepsilon_0$. For pure shear and pure compression, the stress is limited by the shear strength $f_s = sf_t$ and the compressive strength $f_c = cf_t$, respectively.

The damage parameter ω is determined by setting the normal stress $\sigma_n = (1-\omega)E\varepsilon_n$ equal to the stress of an exponential stress crack opening curve of the form $\sigma_n = f_t \exp(w_{cn}/w_f)$. Within this damage formulation, the crack opening is defined as $\mathbf{w}_c = \{w_{cn}, w_{cs}\}^T = \omega h\{\varepsilon_n, \varepsilon_s\}^T$. Replacing ε_n by κ in these two expressions of the normal stress, the nonlinear equation for the stress equilibrium is

$$(1-\omega)E\kappa = f_t \exp\left(-\frac{\omega h\kappa}{w_f}\right) \tag{26}$$

from which the damage parameter ω was determined iteratively using the Newton-Raphson method. Parameter w_f determines the initial slope of the stress crack opening softening curve and is related to the fracture energy $G_F = f_t w_f$ for pure tensile loading, which corresponds to the total area under the stress crack opening curve in Fig. 5b. The model parameters for the structural part are E and γ for the elastic, and ε_0, q, c and w_f for the inelastic response. The present constitutive model is a scalar damage model which reduces the stiffness of the material isotropically. This differs from the axisymmetric model in Section 3 in which only the circumferential stiffness is reduced. Still, the two models provide a good agreement (see Section 5), because the network model is based on a two-dimensional discretisation of the cylinder. Therefore, the

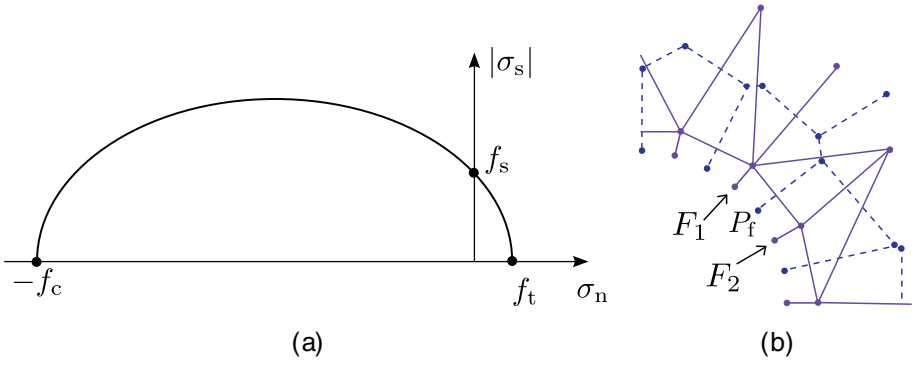

Fig. 5. (a) Network model: elliptic strength envelope in structural stress space and (b) fluid pressure at transport nodes derived from reactive forces associated with applied displacements.

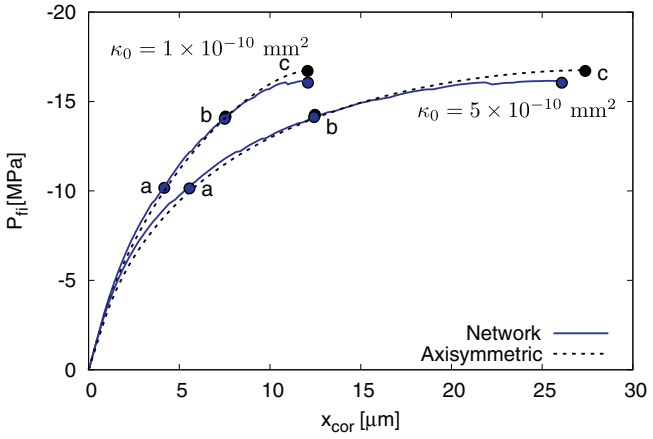

Fig. 6. Internal pressure P_{fi} versus loss of radius x_{cor} for the network and axisymmetric model. The three marked stages refer to crack patterns shown in Fig. 7.

overall anisotropic response is captured by spatially localised zones of isotropic damage.

4.2. Transport model

The lattice model for the fluid transport is based on several idealisations. Fluid pressures applied at the boundary of the model result in steady-state conditions. Thus, any transient effects due to changes of the boundary pressure and changes of the transport properties are disregarded. Instead, the final state, for which equilibrium with the hydraulic boundary conditions hold, is considered. This idealised approach is well suited for applications in which the change of boundary pressure and crack propagation occur slowly. Furthermore, the fluid within the concrete is assumed incompressible.

The transport of an incompressible fluid through a saturated porous medium in steady-state conditions based on mass conservation, laminar flow conditions and Darcy's law, is described by the differential equation

$$\mathrm{div}\,(\kappa/\mu \mathrm{grad} P_f) = 0 \tag{27}$$

κ is the permeability and P_f is the pore fluid pressure (tension positive) already introduced in Section 3.

The differential equation for mass transport in Eq. (27) is modelled by a network of one-dimensional transport elements shown by the dashed lines in Fig. 4. The discrete form of one of these elements is

$$\boldsymbol{\alpha}_e \mathbf{P}_f = \mathbf{f}_e \tag{28}$$

where $\mathbf{P}_f$ is a vector containing the nodal values of the fluid pressure, $\boldsymbol{\alpha}_e$ is the conductivity matrix and $\mathbf{f}_e$ is the nodal flow rate vector. The conductivity matrix is defined as

$$\boldsymbol{\alpha}_e = \frac{A}{l}\kappa/\mu \begin{pmatrix} 1 & -1 \\ -1 & 1 \end{pmatrix} \tag{29}$$

where $A = h$ is the area of the rectangular cross-section assuming a unit thickness in the out of plane direction, and h and l are defined in Fig. 4b. As in Section 3, the permeability κ comprises two parts

$$\kappa = \kappa_0 + \kappa_c \tag{30}$$

where κ_0 is the permeability of the uncracked material and κ_c is the permeability contribution due to cracking which is

$$\kappa_c = \xi \frac{\bar{w}_c^3}{12h} \tag{31}$$

This expression of κ_c differs from Eq. (14) in Section 3, since it does not require any information about the number of cracks, which is determined automatically from the two-dimensional boundary value problem. The variable $\bar{w}_c$ is the equivalent crack opening defined as

$$\bar{w}_c = \sqrt{w_{cn}^2 + w_{cs}^2} \tag{32}$$

The aim of this study was to model cracking caused by the confinement of corrosion products by a coupled transport-structural approach. The coupling was introduced at the steel/concrete interface by setting the structural stress equal to the fluid pressure. This was achieved by converting the radial components of the nodal forces resulting from the eigendisplacement at the interface layer between steel and concrete phase into a fluid pressure by dividing them by the cross-sectional area of the element (Fig. 5b). This pressure is applied to the boundary nodes of the transport model.

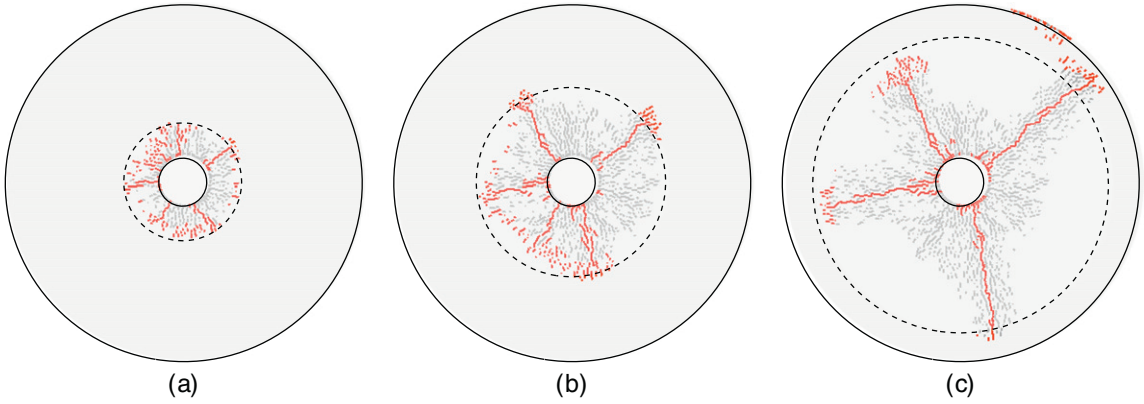

Fig. 7. Crack patterns for three stages in the P_{fi}-x_{cor} curve shown in Fig. 6. The red and grey lines show active and inactive cracks. The dashed line represents the interface between cracked and uncracked regions of the axisymmetric model. (For interpretation of the references to colour in this figure legend, the reader is referred to the web version of this article.)

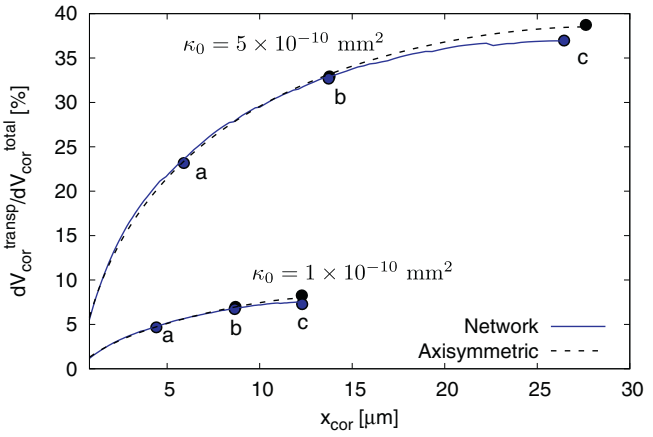

Fig. 8. Ratio of changes of volume of transported and total volume of corrosion products versus radius loss x_{co} for the network and axisymmetric model. The three marked stages refer to crack patterns shown in Fig. 7.

The required input parameters of the transport part of the network model are κ_0, μ and ξ.

5. Comparison between axisymmetric and network model

The two modelling approaches outlined above were applied to the failure process of a thick-walled cylinder subjected to an increasing inner radial displacement representing a layer of corrosion products. The aim of this analysis was to investigate the nonlinear relationship between the radial pressure and loss of diameter x_{cor}, as well as to compare the performances of the axisymmetric and network approaches. The analyses were performed incrementally, whereby for each increment a sequence of structural and transport analyses were performed. Then, x_{cor} was determined by adding the corresponding increments calculated in Eq. (3).

For all analyses, the same input parameters were chosen for the axisymmetric and network model. The geometry of the thick-walled cylinder was chosen as $r_i = 8$ mm and $r_o = 58$ mm. The material parameters for the structural part of both models were Young's modulus $E = 30$ GPa, Poisson's ratio $\nu = 0$, tensile strength $f_t = 3$ MPa and fracture energy $G_F = 0.15$ N/mm. For the network model, the minimum distance for the discretisation was chosen as $d_{min} = 1$ mm. For the axisymmetric model, it was also required to assume the number of cracks, which was chosen as $n_c = 4$ based on preliminary results obtained from the network model. For the transport part, two permeabilities of the uncracked material were used to investigate the influence of this parameter on the loss of radius x_{cor}. The permeabilities were chosen as $\kappa_0 = 1 \times 10^{-10}$ and 5×10^{-10} mm^2. Furthermore, the other parameters for the transport part were selected as $\xi = 0.001$ and $\mu = 0.019$ MPas. Finally, for the calculation of dx_{cor}, the expansion factor of the corrosion products was assumed to be $\alpha = 2$ and $i_{cor} = 100\,\mu$A/cm^2. The permeability value $\kappa_0 = 1 \times 10^{-10}$ mm^2 and tortuosity value $\xi = 0.001$ was used previously in [12] for modelling the influence of cracking on capillary suction in concrete, which provided good agreement with experiments. The greater value $\kappa_0 = 1 \times 5^{-10}$ mm^2 was used here to investigate if the two modelling approaches are capable of taking into account the increase of permeability on the transport of corrosion products. Furthermore, the values for the expansion factor α and the current density i_{cor} are typical for the modelling of accelerated corrosion tests [17].

In Fig. 6, the internal pressure P_{fi} versus the loss of steel radius x_{cor} for the two uncracked permeabilities κ_0 is shown for the two modelling approaches. The agreement between the two approaches is very good. The axisymmetric model only slightly overestimates the maximum pressure obtained by the network model. Furthermore, κ_0 has a strong influence on the P_{fi}-x_{cor} curve. For the greater permeability, the maximum pressure is reached at a greater x_{cor}. Although cracking strongly influences the P_{fi}-x_{cor} curve resulting in the nonlinear structural response, it was found to have a small influence on the overall permeability of the transport part despite crack openings at the steel concrete interface $w_c^{max} \approx 0.1$ mm. The reason for this small influence is that the outer boundary layer of the thick-walled cylinder was not cracked yet. Therefore, the crack path for fluid to the surface is not continuous. Once the crack reaches the surface, the influence of cracking increases significantly. This trend is a natural result of the present model, since it is able to take into account the connectivity of the crack with the outer surface. This is one of the advantages of the present approach over models, which fill cracks with corrosion products based on adhoc rules. For the axisymmetric model, the case of the crack joining the outer surface was not considered, since it violates the assumption of smeared out damage in the circumferential direction.

In Fig. 6, three stages are marked at which the cracking predicted by the network model is shown in Fig. 7. The red and grey lines (see online version for colours) refer to active and inactive cracks, respectively. Here, an active crack is visualised as a mid-cross-section of a

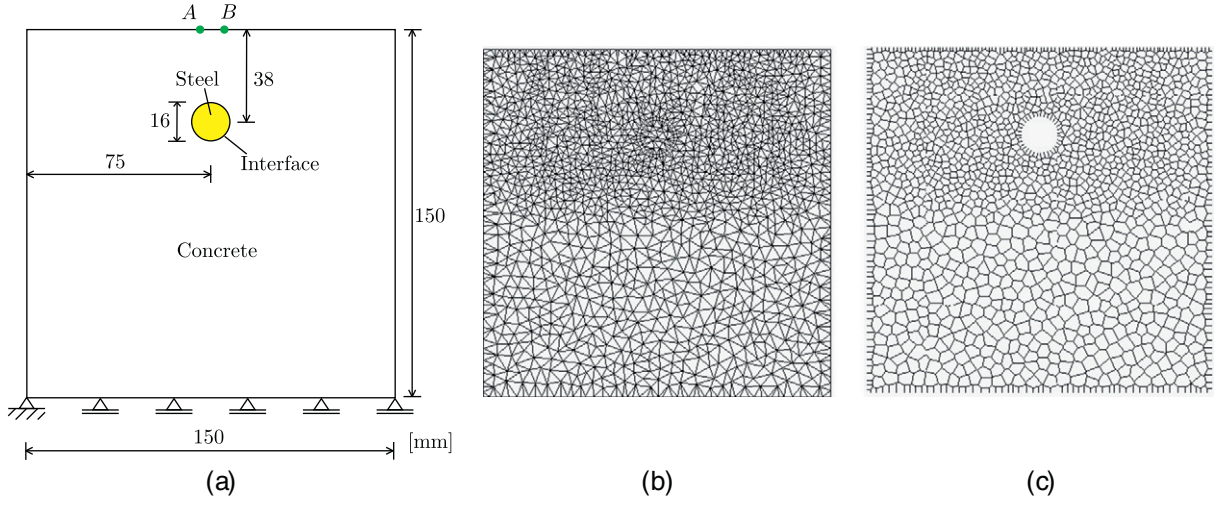

Fig. 9. Concrete specimen containing a single reinforcing bar: (a) geometry, and (b) structural and (c) transport network.

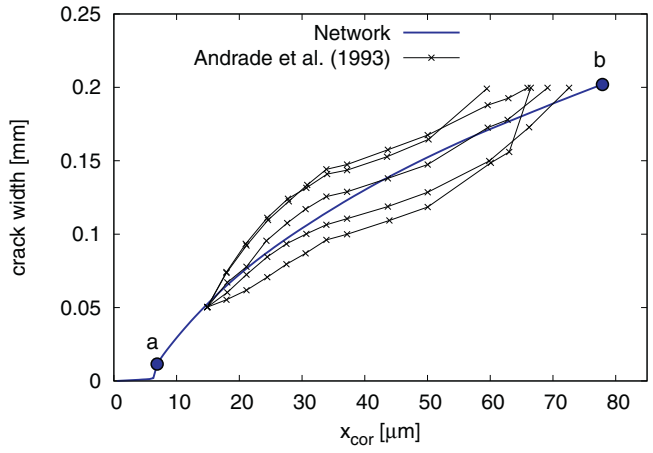

Fig. 10. Corrosion induced cracking for a single reinforcement bar: comparison between numerical and experimental results from Andrade et al. [2]. Stages (a) and (b) refer to the crack patterns shown in Fig. 11.

structural element for which the damage variable increases at this stage of analysis. The dashed line shows the interface between the crack and uncracked region predicted by the axisymmetric model. It can be seen that there is again a very good agreement between the axisymmetric and network model. For stage (c), the four main cracks from the network model do not have the same length anymore. This indicates the limit of the axisymmetric model. Any further radial displacement at the inner boundary, would lead to a completely asymmetric crack pattern with only one crack remaining active. The crack patterns in Fig. 7 apply to both analyses ($\kappa_0 = 1 \times 10^{-10}$ and 5×10^{-10} mm^2), since the structural part of the analysis is independent of the transport part.

The strong influence of the permeability κ_0 on the amount of transported corrosion products is further illustrated by showing the ratio of increments of transported and total volumes of corrosion products versus the loss of radius for the two models in Fig. 8. Again, a good agreement between the models is obtained. The greater the permeability, the greater is the volume of corrosion products transported into the concrete. At stage (c), the volume ratio predicted from the axisymmetric model is slightly greater than that from the network approach, since also the inner pressure of the axisymmetric model is greater than the network one.

The good agreement between the axisymmetric and network models gives confidence in the ability of the models to describe the considered processes correctly. In the next step, the network model is used to analyse the response of structures with more complicated geometries for which the axisymmetric model could not be used since the assumptions of axisymmetry do not hold anymore.

6. Calibration

Since the approach for modelling corrosion induced cracking as a coupled transport-structural problem is new, there is not enough information in the literature for choosing the dynamic viscosity of the corrosion products, which is modelled as a fluid. Here, the dynamic viscosity of the corrosion products is inversely calibrated by fitting the experimental time versus crack opening results for a specimen with a single reinforcement bar reported in Andrade et al. [2]. It is assumed that the dynamic viscosity is time independent. The geometry and loading setup of the concrete specimen with a single reinforcement bar is shown in Fig. 9. The out-of plane thickness of the specimen is 380 mm. The crack opening was defined as the relative horizontal displacement between the two nodes *A* and *B* at the top of the specimen shown in Fig. 9. For the transport model, the specimen is assumed to be fully saturated. Furthermore, the pressure along the external boundaries of the specimen is assumed to be zero. Model input parameters for three phases, namely concrete, steel and interface between steel and concrete are required for the structural part. For the transport part, the steel is assumed to be impermeable. Therefore, it is not discretised by the network of transport elements. The 2D networks used for the analysis are shown in Fig. 9b and c.

For concrete, the input parameters for the structural part are $E = 37$ GPa, $f_t = 3.2$ MPa, $G_F = 143$ J/m^2, $\gamma = 1$. These parameters were determined according to FIB [10]. The steel is modelled to behave elastically with $E = 210$ GPa [17] and $\gamma = 1$. The exact value of the Young's modulus of steel is of minor importance, as long as it is much higher than the one of the concrete. The interface between steel and concrete was assumed to have the same properties as concrete, except for the ratio of the normal and shear stiffness which was set to $\gamma = 0.0001$. This low value was

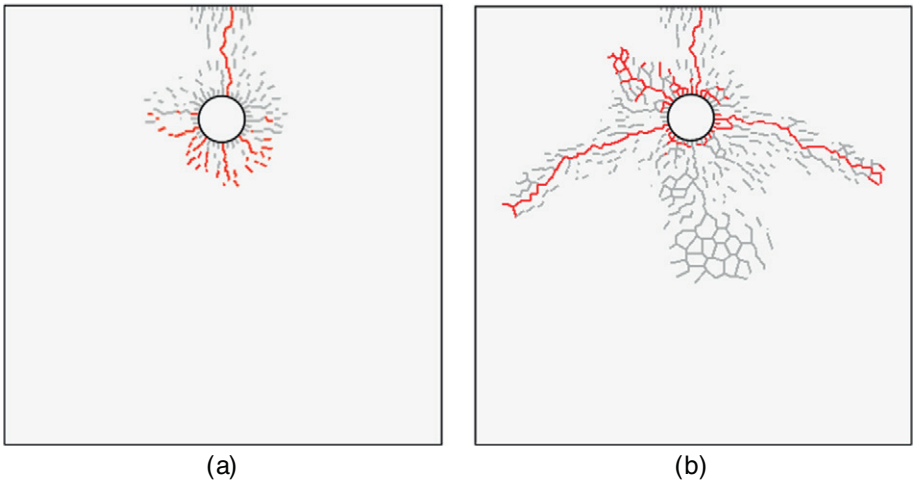

Fig. 11. Corrosion induced cracking for a single reinforcement bar: fracture patterns obtained during analyses for (a) $x_{cor} = 6.87\,\mu$m and (b) 77.3 μm. Red lines indicate mid-cross-sections of network elements in which damage increases at this stage of analysis. Grey lines represent mid-cross-sections of elements at which damage is present but does not increase at this stage of analysis. (For interpretation of the references to colour in this figure legend, the reader is referred to the web version of this article.)

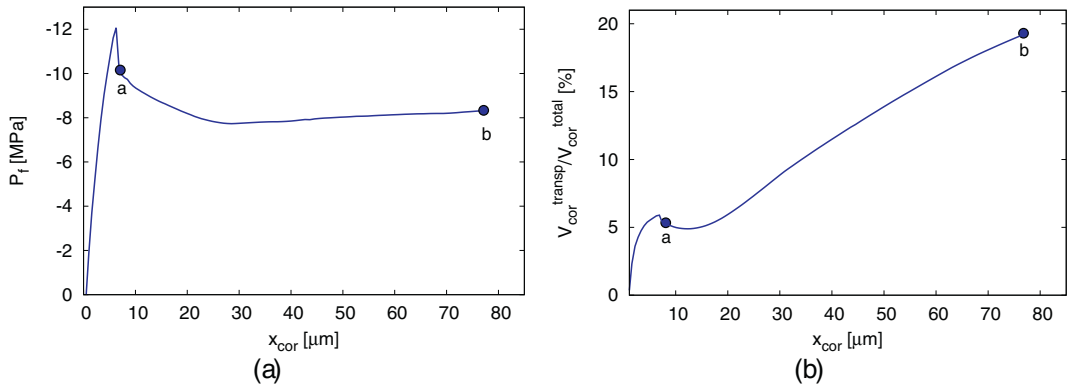

Fig. 12. Corrosion induced cracking for a single reinforcement bar: (a) average fluid pressure along the steel/concrete boundary and (b) percentage of corrosion products penetrating pores and micro-cracks. Stages (a) and (b) refer to the crack patterns shown in Fig. 11.

chosen so that cracks at the steel-concrete interface could open. The transport parameters were chosen as $\kappa_0 = 1 \times 10^{-10}$ mm^2, $\xi = 0.001$ and $\mu = 0.019$ MPas. In structural examples in which potentially spalling of the concrete cover occurs, the crack opening, and thus crack permeability in the transport model, can be very large. Therefore, for all analyses in Sections 6 and 7, the upper limit for the crack permeability was calculated for an upper limit of the equivalent crack opening $\bar{w}_c = 0.05$ mm to avoid numerical problems. The parameters, κ_0 and ξ were chosen from a previous study in [12]. On the other hand, the dynamic viscosity was determined by fitting the experimental results shown in Fig. 10. The model parameters for the corrosion products were chosen as $\alpha = 2$ and $i_{cor} = 100\mu$A/cm^2 according to the experiments in Andrade et al. [2].

For the comparison with the experimental results in Fig. 10, the experimental results were aligned with the numerical results at an attack penetration depth $x_{cor} = 14.9\mu$m, which was the reported corrosion at the start of the test of Andrade et al. [2].

The crack patterns at $x_{cor} = 6.87\,\mu$m and 77.3 μm (corresponding to stages (a) and (b) in Fig. 10) are shown in Fig. 11a and b, respectively.

The pressure at the steel concrete interface versus the loss of radius x_{cor} is shown in Fig. 12a. Furthermore, the ratio of transported and total volumes of corrosion products versus the loss of radius x_{cor} is shown in Fig. 12b.

After surface cracking occurs (Fig. 11a), the pressure drops initially. However, one crack connected to the surface is not sufficient to cause the complete failure of the specimen. Therefore, with increasing steel radius loss, the pressure increases again which is accompanied by a propagation of multiple additional cracks into the specimen. The formation of the surface crack is initially associated with a decrease of the ratio of transported and total volume of corrosion products due to the pressure drop. However, with increasing opening of the crack connected to the specimen surface this ratio increases strongly. Thus, the increase of permeability due to the increasing crack opening has a stronger influence than the reduction of pressure.

7. Comparison with experiments

Next, the proposed coupled approach was applied to the prediction of crack widths in a rectangular slab (specimen III-20-16 in Mullard and Stewart [19]) containing four equally spaced reinforcing bars (Fig. 13a). Again, the eigendisplacement that represents the structural corrosion layer is applied to the interface elements along the boundary between the reinforcement bar and concrete for each of the four reinforcement bars. The crack width, w_c is taken as the relative horizontal displacement between two nodes A and B at the top of the specimen above the most right-hand reinforcement bar location in Fig. 13a. The out-of-plane thickness of the specimen is 1000 mm. The structural and transport networks used for the analysis are shown in Fig. 13b and c, respectively.

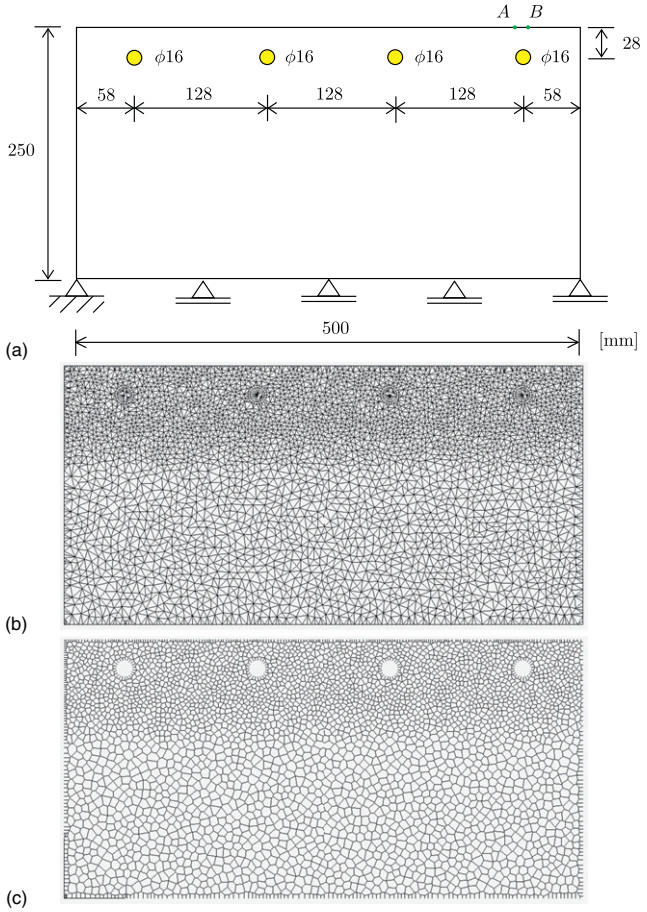

Fig. 13. Concrete specimen containing four reinforcing bars: (a) geometry and loading setup according to [19], and (b) structural and (c) transport network.

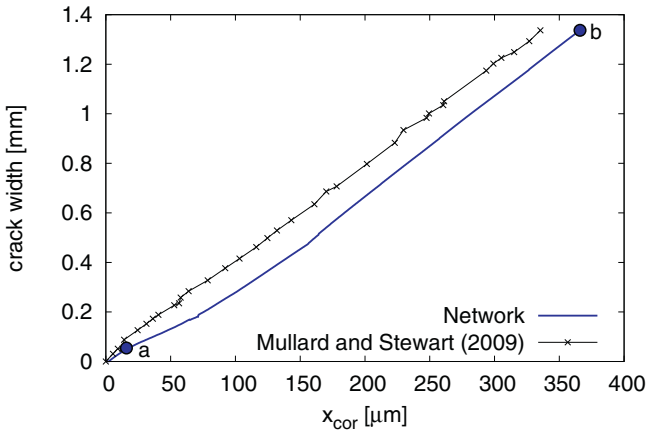

Fig. 14. Corrosion induced cracking of multiple reinforcement bars: comparison of crack width w_c versus radius loss x_{cor} from the network model and experiments reported in [19].

For concrete, the model parameters for the structural part were again determined using FIB [10] based on the experimental results in Mullard and Stewart [18]. The parameters were $E = 39.4$ GPa, $f_t = 2.4$ MPa, $G_F = 135.8$ J/m^2, $\gamma = 1$. The steel was modelled to behave elastically with $E = 210$ GPa and $\gamma = 1$. As in Section 6, the interface between steel and concrete was assumed to have the same properties as concrete, except for the ratio of the normal and shear stiffness which was set to a low value of $\gamma = 0.0001$. The transport parameters were chosen to be same as for the single reinforcement bar specimen in Section 6 which were $\kappa_0 = 1 \times 10^{-10}$ m^2, $\xi = 0.001$ and $\mu = 0.019$ MPas. The model parameters for the corrosion products were chosen again as $\alpha = 2$ and $i_{cor} = 100\mu$A/cm^2, as it was done in Section 6.

In Fig. 14, the comparison between the numerical and the experimental results from Mullard and Stewart [18] is shown in the form of crack opening w_c versus radius loss x_{cor}. Overall, a good agreement was obtained.

The crack patterns at $x_{cor} = 16.4\mu$m and 366.1 μm are shown in Fig. 15a and b, respectively.

The average fluid pressure along the steel/concrete versus the loss of radius x_{cor} is shown in Fig. 16a. Furthermore, the ratio of transported and total volumes of corrosion products versus the loss of radius x_{cor} is shown in Fig. 16b.

The crack patterns in Fig. 15 show that initially the cracks reach the surface. Upon further corrosion, the cracks around the individual reinforcement bars join up. At the end of the analysis, the crack formation indicates spalling of the concrete surface. The crack propagation is accompanied by significant pressure drop. However, because of the severe cracking the increase in permeability is so great that the ratio of transported and total ratio still increases despite the pressure drop. At a radius loss of $x_{cor} = 100\mu$m, the ratio decreases which is due to a combination of the further reduction in pressure and the imposed upper limit on the permeability which was applied to the structural analyses in the present section and Section 6

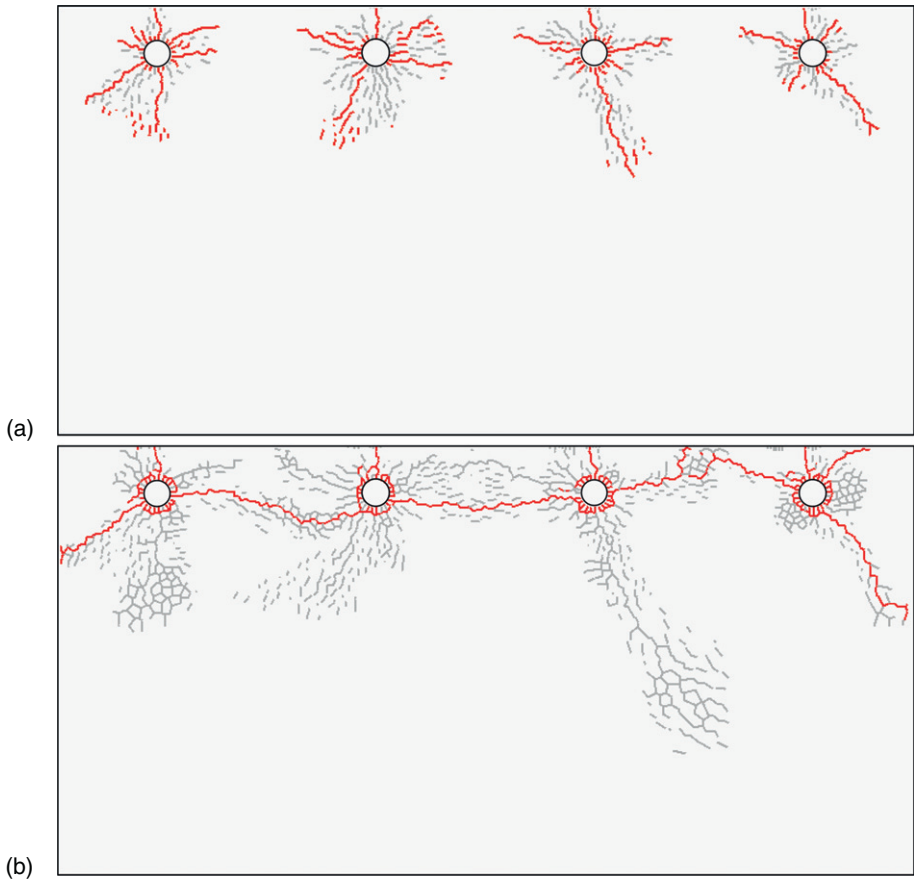

Fig. 15. Corrosion induced cracking for multiple reinforcement bars: fracture patterns for x_{cor} values of (a) 16.4 μm and (b) 366.1 μm. Red lines indicate mid-cross-sections of network elements in which damage increases at this stage of analysis. Grey lines represent mid-cross-sections of elements at which damage is present but does not increase at this stage of analysis. (For interpretation of the references to colour in this figure legend, the reader is referred to the web version of this article.)

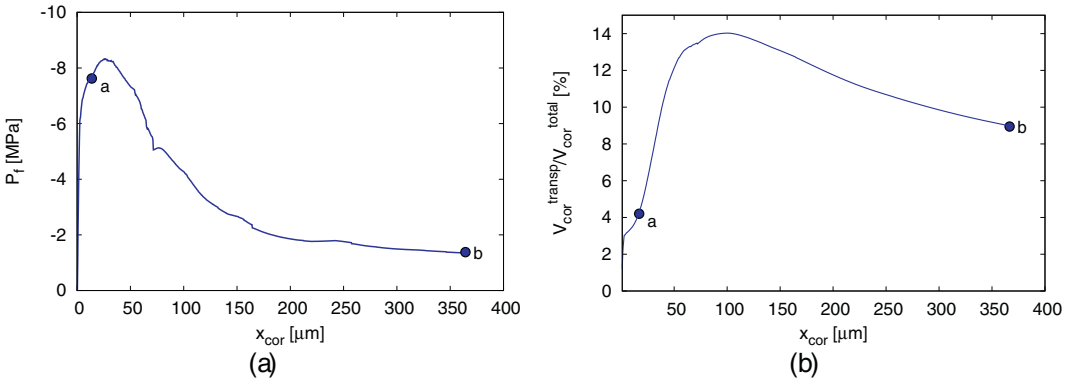

Fig. 16. Corrosion induced cracking for multiple reinforcement bars: (a) average fluid pressure along the steel/concrete boundary and (b) percentage of corrosion products penetrating pores and micro-cracks. Stages (a) and (b) refer to the crack patterns shown in Fig. 15.

to avoid computational problems. Without this upper limit on the permeability it would be expected that the ratio is monotonically increasing.

8. Conclusion

A new transport-structural modelling approach to corrosion induced cracking has been proposed, which includes the pressure driven transport of corrosion products. This approach has been applied to both an axisymmetric thick-walled cylinder model and a network model. The results of the two models are in very good agreement in the form of pressure versus radius loss, crack fronts and transported volumes versus radius loss. Whereas the axisymmetric thick-walled cylinder model is only valid up to the peak of the pressure-radius loss curves, the network model has the potential to predict the entire propagation phase up to spalling.

The present coupled transport mechanical model is a research tool which is intended, together with detailed experiments, to improve the understanding of corrosion induced cracking. This understanding can then be used to develop design charts which can be applied to the prediction of the deterioration of reinforced concrete structures undergoing corrosion induced cracking. Future research will focus on determining the spatial distribution of corrosion products around reinforcement bars. Furthermore, more research is required to investigate the interplay of the expansion factor, current density and dynamic viscosity parameters used in the present study.

Acknowledgments

The numerical analyses were performed with the nonlinear analyses program OOFEM [22] extended by the present authors. P. Grassl acknowledges funding received from the UK Engineering and Physical Sciences Research Council (EPSRC) under grant EP/I036427/1 and funding from Radioactive Waste Management Limited (RWM) (http://www.nda.gov.uk/rwm), a wholly-owned subsidiary of the Nuclear Decommissioning Authority. RWM is committed to the open publication of such work in peer reviewed literature, and welcomes e-feedback to rwmdfeedback@nda.gov.uk.

References

[1] C. Alonso, C. Andrade, J. Rodriguez, J. Diez, Factors controlling cracking of concrete affected by reinforcement corrosion, Mater. Struct. 31 (7) (1998) 435–441.
[2] C. Andrade, C. Alonso, F.J. Molina, Cover cracking as a function of bar corrosion part i-experimental test, Mater. Struct. 26 (8) (1993) 453–464.
[3] Z.P. Bažant, Physical model for steel corrosion in concrete sea structures: application, J. Struct. Div. ASCE 105 (6) (1979) 1154–1166.
[4] J.E. Bolander, S. Berton, Simulation of shrinkage induced cracking in cement composite overlays, Cem. Concr. Compos. 26 (2004) 861–871.
[5] J.E. Bolander, S. Saito, Fracture analysis using spring networks with random geometry, Eng. Fract. Mech. 61 (1998) 569–591.
[6] J.P. Broomfield, Corrosion of Steel in Concrete: Understanding, Investigation and Repair, Taylor & Francis. 1997.
[7] L. Chernin, D.V. Val, K.Y. Volokh, Analytical modelling of concrete cover cracking caused by corrosion of reinforcement, Mater. Struct. 43 (4) (2010) 543–556.
[8] B. Damjanac, C. Detournay, P.A. Cundall, Application of particle and lattice codes to simulation of hydraulic fracturing, Comput. Part. Mech. (2015) 1–13.
[9] T. El Maaddawy, K. Soudki, A model for prediction of time from corrosion initiation to corrosion cracking, Cem. Concr. Compos. 29 (3) (2007) 168–175.
[10] FIB, FIB-Model Code for Concrete Structures 2010, International Federation for Structural Concrete (FIB). 2012.
[11] P. Grassl, A lattice approach to model flow in cracked concrete, Cem. Concr. Compos. 31 (7) (2009) 454–460.
[12] P. Grassl, C. Fahy, D. Gallipoli, J.E. Bolander, A lattice model for fracture and mass transport in concrete, Proceedings of Microdurability, The Netherlands, 2012.
[13] P. Grassl, C. Fahy, D. Gallipoli, S.J. Wheeler, On a 2D hydro-mechanical lattice approach for modelling hydraulic fracture, J. Mech. Phys. Solids 75 (2015) 104–118.
[14] Y. Liu, R. Weyers, Modeling the time-to-corrosion cracking in chloride contaminated reinforced concrete structures, ACI Mater. J. 95 (6) (1998) 675–680.
[15] K. Lundgren, Bond between ribbed bars and concrete. Part 2: the effect of corrosion, Mag. Concr. Res. 57 (7) (2005) 383–395.
[16] A. Michel, B.J. Pease, A. Peterová, M.R. Geiker, H. Stang, A.E.A. Thybo, Penetration of corrosion products and corrosion-induced cracking in reinforced cementitious materials: experimental investigations and numerical simulations, Cem. Concr. Compos. 47 (2014) 75–86.
[17] F. Molina, C. Alonso, C. Andrade, Cover cracking as a function of rebar corrosion: part II-numerical model, Mater. Struct. 26 (9) (1993) 532–548.
[18] A. Mullard, M.G. Stewart, Corrosion-induced cover cracking: new test data and predictive models, ACI Struct. J. 108 (1) (2011) 71.
[19] J.A. Mullard, M.G. Stewart, Corrosion-induced cover cracking of RC structures: new experimental data and predictive models, Technical Report University of Newcastle. 2009.
[20] J. Ožbolt, F. Oršanić, G. Balabanić, M. Kušter, Modeling damage in concrete caused by corrosion of reinforcement: coupled 3D FE model, Int. J. Fract. 178 (1–2) (2012) 233–244.
[21] S.J. Pantazopoulou, K.D. Papoulia, Modeling cover-cracking due to reinforcement corrosion in RC structures, J. Eng. Mech. 127 (4) (2001) 342–351.
[22] B. Patzák, OOFEM - an object-oriented simulation tool for advanced modeling of materials and structures, Acta Polytechnica 52 (2012) 59–66.
[23] B. Šavija, M. Luković, J. Pacheco, E. Schlangen, Cracking of the concrete cover due to reinforcement corrosion: a two-dimensional lattice model study, Construct. Build Mater. 44 (2013) 626–638.
[24] B. Šavija, M. Luković, S.A.S. Hosseini, J. Pacheco, E. Schlangen, Corrosion induced cover cracking studied by X-ray computed tomography, nanoindentation, and energy dispersive X-ray spectrometry (EDS), Mater. Struct. 48 (7) (2015) 2043–2062.
[25] E. Schlangen, J.G.M. van Mier, Simple lattice model for numerical simulation of fracture of concrete materials and structures, Mater. Struct. 25 (1992) 534–542.
[26] K. Toongoenthong, K. Maekawa, Simulation of coupled corrosive product formation, migration into crack and propagation in reinforced concrete sections, J. Adv. Concr. Technol. 3 (2) (2005) 253–265.

[27] K. Tran, H. Nakamura, K. Kawamura, M. Kunieda, Analysis of crack propagation due to rebar corrosion using RBSM, Cem. Concr. Compos. 33 (9) (2011) 906–917.
[28] K. Tuutti, Corrosion of Steel in Concrete, doctoral thesis. Swedish Cement and Concrete Research Institute. 1982.
[29] A.C. Ugural, S.K. Fenster, Advanced Strength and Applied Elasticity. The SI Version Edward Arnold, 1981.
[30] P.A. Witherspoon, J.S.Y. Wang, K. Iawai, J.E. Gale, Validity of cubic law for fluid flow in a deformable rock fracture, 16 (6) (1980) 1016–1024.
[31] H.S. Wong, Y.X. Zhao, A.R. Karimi, N.R. Buenfeld, W.L. Jin, On the penetration of corrosion products from reinforcing steel into concrete due to chloride-induced corrosion, Corros. Sci. 52 (2010) 2469–2480.
[32] Y. Zhao, A.R. Karimi, H.S. Wong, B. Hu, N. Buenfeld, W. Jin, Comparison of uniform and non-uniform corrosion induced damage in reinforced concrete based on a Gaussian description of the corrosion layer, Corros. Sci. 53 (9) (2011) 2803–2814.